Geomagnetic Conjugate Observations of Ionospheric Disturbances in response to North Korea Underground Nuclear Explosion on 3 September 2017

Yi Liu, Chen Zhou[*], Qiong Tang, Guanyi Chen, and Zhengyu Zhao

Department of Space Physics, School of Electronic Information, Wuhan University, Wuhan, China

Corresponding to: chenzhou@whu.edu.cn

Key points:

1. Geomagnetic conjugate ionospheric disturbances related to UNE were observed by IGS stations and Swarm satellite.

2. Radial propagation velocity from the UNE epicenter was calculated from temporal and spatial distribution of conjugate ionospheric disturbances.

3. The ionospheric disturbances present the evidence of the LAIC electric field penetration process.

Abstract

We report observations of ionospheric disturbances in response to North Korea underground nuclear explosion (UNE) on 3 September 2017. By using data from IGS (International GNSS Service) stations and Swarm satellite, geomagnetic conjugate ionospheric disturbances were observed. The observational evidences showed that UNE-generated ionospheric disturbances propagated radially from the UNE epicenter with the velocity of ~ 280 m/s. We propose that the ionospheric disturbances are results of electrodynamic process caused by LAIC (Lithosphere-Atmosphere-Ionosphere Coupling) electric field penetration. LAIC electric field can also be mapped to the conjugate hemispheres along the magnetic field line and consequently cause ionospheric disturbances in conjugate regions. The UNE-generated LAIC electric field penetration plays an important role in the ionospheric disturbances in the region of the nuclear test site nearby and the corresponding geomagnetic conjugate points.

Key words: geomagnetic conjugate ionospheric disturbances; electrodynamic process; LAIC electric field penetration

1 Introduction

Ionospheric disturbances can be generated by various natural processes such as geomagnetic storms, internal electrodynamic instabilities and so forth. Furthermore, human activity can also cause evident ionospheric disturbances. Although underground nuclear explosion (UNE) is detonated deep in the lithosphere, ionospheric disturbances related to UNE can also be observed. By using GNSS-TEC observations, *Park et al.* (2011) reported that traveling ionospheric disturbances (TIDs) with phase velocity of ~273 m/s were generated by UNE in the 25 May 2009 North Korea UNE test. They proposed that acoustic gravity waves (AGWs) generated by the UNE can propagate to ionosphere and cause wavelike disturbances.

While the observations of UNE related ionospheric disturbances have been discussed in (*Park et al.*, 2011; 2013), further investigation is still required to understand the mechanism(s) of ionospheric disturbance generation. Lithosphere-atmosphere-ionosphere coupling (LAIC) mechanisms originally proposed to interpret the linkage between ionospheric disturbances and earthquake activities are the most likely explanation for the ionospheric disturbances in response to UNE. The AGWs theory is one part of LAIC mechanisms (*Liu et al.*, 2016; *Maruyama et al.*, 2016). AGWs excited by the unusual events in lithosphere such as an earthquake or an UNE can propagate to ionospheric height and generate TID and electromagnetic disturbances (*Gokhberg et al.*, 1990; *Pokhotelov et al.*, 1994, 1995, 1999; *Mikhailov et al.*, 2000; *Huang et al.*, 2011; *Jonah et al.*, 2017). However, the AGWs mechanism cannot fully explain all the

3

56 observations related to earthquakes. The electrostatic coupling is another candidate for

57 LAIC mechanisms. During earthquakes, LAIC electric filed or current can be excited

58 by complex physical and chemical reactions induced by rock rupture and penetrate the

59 ionosphere to promote plasma disturbances by $E \times B$ motion (*Xu et al.*, 2011; *Zhao &*

60 *Hao*, 2015). *Zhou et al.* (2017) developed an electric field penetration model for LAIC

61 and their simulation results showed that the penetration height of LAIC electric field

62 can reach to 400 km in mid-latitude regions. Because of high electric conductivity along

63 the geomagnetic field lines, LAIC electric field can also be mapped along geomagnetic

64 field lines and cause ionospheric disturbances at the geomagnetic conjugate points

65 (*Ruzhin et al.*, 1998; *Zhang et al., 2009*; *Li & Parrot*, 2017).

66

67 In this study, we have used magnetic conjugate GNSS observations and Swarm satellite

68 to investigate the LAIC electric penetration effects of North Korea UNE on 3

69 September 2017.

70

71 **2 Instrument and Data**

72 The IGS stations used in this study are located in East Asia and Australia. The

73 geographical positions of the UNE and the IGS stations are showed in Figure 1. In order

74 to eliminate the noise and multipath effects of GPS signals, only carrier phase

75 observations are utilized to derive the relative slant total electron content (STEC). The

76 time resolution is about 30 s. The ionospheric pierce points (IPPs) height in this study

77 is assumed at 350 km. Figure 2 shows an example of time series of relative STEC

78 obtained by SUWN using satellite PRN 28 between 03:00-05:00 UT on 3 September

79 2017. To calculate the ionospheric disturbances related to UNE from GNSS

80 observations, the main trends of relative STEC strongly influenced by the Sun's diurnal

81 cycle need to be removed. In this study, the numerical third-order horizontal 3-point

82 derivatives of relative STEC are used for extracting the ionospheric disturbances (*Park*

83 *et al.*, 2011). In the first step, the numerical first-order horizontal 3-point derivatives

84 are taken as follows:

85 $$\delta s_i = s_i - \frac{\left(s_{i-1} + s_{i+1}\right)}{2} \qquad i=\{2,...,n\text{-}1\} \tag{1}$$

86 where s_i is the ith data point, δs_i is the first derivative, and n is the number of relative

87 STEC observations. The main relative STEC trends are removed through this process.

88 Figure 3(a) shows the time series of first-order derivatives of relative STEC. Waves

89 with small amplitudes occurred at around 3.9 and 4.1 hours, even though it was not

90 certain whether they were meaningful signals or just noises. The numerical derivative

91 formula is repeatedly performed on relative STEC derivatives to extract the ionospheric

92 disturbances related to UNE. The second-order derivatives can be written in the

93 following expression:

94 $$\delta\delta s_i = \delta s_i - \frac{\left(\delta s_{i-1} + \delta s_{i+1}\right)}{2} \qquad i=\{2,...,m\text{-}1\} \tag{2}$$

95 where $\delta\delta s_i$ is the second derivative, and m is the number of first derivative

96 observations. Figure 3(b) shows the time series of second-order derivatives of relative

97 STEC. Compared to the first-order derivatives presented in Figure 3(a), the amplitude

98 around the 3.9 hour was amplified while others were not significant. The third-order

99   derivatives are given as follows:

100      $$\delta\delta\delta s_i = \delta\delta s_i - \frac{(\delta\delta s_{i-1} + \delta\delta s_{i+1})}{2} \quad i=\{2,...,l-1\} \tag{3}$$

101   where $\delta\delta\delta s_i$ is the third derivative, and l is the number of second derivative

102   observations. Figure 3(c) shows the time series of third-order derivatives of relative

103   STEC. Compared to the second-order derivatives presented in Figure 3(b), the

104   disturbances around the 3.9 hour was further amplified. Therefore, compared to the

105   standard first derivatives, the numerical third-order horizontal –point derivatives can

106   emphasized the more significant wave components with small amplitudes. Moreover,

107   to further remove the background noises of third-order derivatives of relative STEC,

108   the harr wavelet decomposition process is applied to the third-order derivatives.

109   Equations (4) and (5) give the harr wavelet function and scale function, respectively.

110      $$\psi_H(t) = \begin{cases} 1 & 0 \leq t \leq 1/2 \\ -1 & 1/2 \leq t < 1 \\ 0 & \text{others} \end{cases} \tag{4}$$

111      $$\phi_H(t) = \begin{cases} 1 & 0 \leq t < 1 \\ 0 & \text{others} \end{cases} \tag{5}$$

112   Figure 3(d) shows the wavelet de-noised third-order derivatives. From Figure 3(d), it

113   was found that the background noises in Figure 3(c) were completely removed and only

114   valuable wave components were retained.

115

116   Swarm mission operated by the European Space Agency (ESA) mainly focuses on the

117   survey of global geomagnetic field and its temporal evolution. Swarm mission consists

118   of three satellites named Alpha (A), Bravo (B), and Charlie (C). By using the magnetic

field data detected by Vector Field Magnetometer (VFM) on Swarm, the ionospheric

radial current (IRC) density could be calculated by using spatial gradient of residual

magnetic field data through Ampère's law (*Ritter et al.*, 2013). The field-aligned current

(FAC) density could be also obtained by the ratio of the IRC density to the sine of the

magnetic inclination angle. The FAC density and IRC density used in the study were

provided by Swarm level 2 dataset with a time resolution of 1 s. The ionospheric current

disturbances associated with UNE can also be calculated by the above method.

3 Observations

According to the measurements of China Earthquake Network Center (CENC), the

approximate location of UNE on 3 September, 2017 is at 41.35 °N and 129.11 °E. The

explosive time was at 03:30:01 UTC. The geomagnetic Kp index was less than 3 and

AE index was less than 500 nT before and after the UNE, which indicates that the

geomagnetic activity was not so active.

Figure 4 shows the time sequences of 3rd-order derivatives of carrier phase derived

relative STEC by GNSS observations from different IGS stations in East Asia and

Australia on 3 September 2017. All the GNSS observations from northern and southern

hemisphere showed obvious short-period fluctuations within 2 hours after the UNE. It

was also found that time delay after the UNE was different according to different IPPs

of GPS signals. Figure 5 presents the IPPs tracks of relative STEC derivatives. In order

to investigate the propagation velocity of ionospheric disturbances, we assumed that

7

141   the UNE-generated ionospheric disturbances propagate radially with a certain velocity.

143   Figure 6 illustrates the satellite Swarm B ionospheric current derivatives. Compared to

144   observed results of ionospheric current in quiet time, it was seen that the FAC

145   derivatives and IRC derivatives at conjugate hemispheres both showed obvious short-

146   period fluctuations after the UNE. The ionospheric current disturbances could reach 0.5

147    $\mu A \cdot m^{-2} \cdot s^{-3}$.

149   Based on the UNE-IPPs horizontal distances and the ionospheric disturbances arrival

150   time, the horizontal propagation velocity of ionospheric disturbances could be

151   estimated by linear fitting model. The horizontal distance from IPPs to epicenter and

152   time delay of the UNE-generated ionospheric disturbances (STEC disturbances and

153   ionospheric current disturbances) are presented in Figure 7. Black triangle and green

154   triangle presented in Figure 7 represent the position of ionospheric current disturbances

155   in the northern hemisphere and the geomagnetic conjugate position of ionospheric

156   current disturbances in the southern hemisphere, respectively. The value of horizontal

157   velocity obtained by the least square estimation was ~280 m/s.

159   **4 Discussion**

160   By utilizing geomagnetic conjugate GNSS TEC observations and ionospheric current

161   products from Swarm, we introduced the ionospheric disturbances which are

162   considered as a result of the UNE carried out by North Korea on 3 September 2017.

163   The method of the numerical third-order horizontal 3-point derivatives was applied to

164   the GNSS TEC and the ionospheric current of Swarm to extract the ionospheric

165   disturbances, which can also be found in *Park et al.*, (2011). Ionospheric disturbances

166   derived from GNSS TEC observations in our study are consistent with the results of

167   North Korea UNE on 25 May 2009 obtained by *Park et al.* (2011).

168

169   The effects of UNE on the ionosphere could be very similar to that of earthquakes on

170   the ionosphere. In previous studies, AGWs are considered as the most likely mechanism

171   for atmospheric and ionospheric disturbances excited by UNE or earthquakes

172   (*Mikhailov et al.*, 2000; *Che et al.*, 2009; *Garrison et al.*, 2010; *Park et al.*, 2011, 2013;

173   *Yang et al.*, 2012; *Maruyama et al.*, 2016). *Klimenko et al.* (2011) proposed that the

174   ionospheric disturbances were generated by small-scale internal gravity waves (IGWs)

175   through propagation and dissipation processes during seismic activity. *Liu et al.* (2016),

176   and *Chum et al.* (2016, 2018) suggested that co-seismic ionospheric disturbances could

177   be generated by long-period infrasound waves excited by seismic waves. Based on

178   GNSS receiver observations over Brazilian sector, *Jonah et al.* (2017) presented

179   daytime MSTIDs observed in the conjugate hemispheres. They proposed that the

180   gravity wave-induced polarized electric fields could map into the conjugate hemisphere

181   and further generate ionospheric disturbances in conjugate region. However, compared

182   with TEC disturbances induced by MSTIDs presented in *Jonah et al.* (2017),

183   ionospheric disturbances in response to North Korea UNE in both hemispheres were

184   smaller and lasted within 5 minutes in our work. Therefore, electric field disturbances

185   induced by UNE-generated TEC disturbances presented in Figure 4 may be very small

186   and cannot generate obvious ionospheric disturbances in conjugate region.

187

188   Recent researches have shown that earthquake ionospheric disturbances could be

189   attributed to not only the AGW mechanism but also the electrostatic coupling, which

190   means the electric field or current penetration into ionosphere induced by earthquakes.

191   Based on the observations of INTERCOSMOS-BULGARIA-1300 satellite and

192   DEMETER satellite, *Gousheva et al.* (2008, 2009) and *Zhang et al.* (2014) reported

193   ionospheric quasi-static electric field perturbations during seismic activities. By using

194   the magnetometer observations, *Hao et al.* (2013), and *Liu et al.* (2016) showed obvious

195   ionospheric current and magnetic field perturbations after the Tohoku earthquake. They

196   proposed that the seismo-traveling atmospheric disturbances (STADs) caused by

197   infrasonic waves can propagate vertically into the ionosphere and modify the E layer

198   Hall and Pedersen conductivity, resulting in background ionospheric electric field and

199   magnetic field disturbances. *Pulinets et al.* (2000) proposed a quasi-electrostatic model

200   for the LAIC mechanism. The simulation results indicated that the abnormal electric

201   field induced by an earthquake can penetrate into the ionosphere to cause the

202   ionospheric electric field disturbances (*Sorokin et al.*, 2001). The enhancement of TEC

203   at the epicenter and its geomagnetic conjugate points were reported by *Liu et al.* (2011),

204   which indicated that the earthquake-generated electric field penetration can be mapped

205   along geomagnetic field lines to promote ionospheric disturbances at its conjugate

206   points by electrodynamic process through $\boldsymbol{E} \times \boldsymbol{B}$ drift. Therefore, the geomagnetic

207 conjugation effects of ionospheric disturbances in Figure 4 can be explained by the

208 UNE-generated electric field penetration. A schematic sketch of geomagnetic conjugate

209 effect related to UNE in the region of the nuclear test site nearby and the corresponding

210 geomagnetic conjugate region is shown in Figure 8. The UNE-generated electric field

211 or current penetrates into the ionosphere and further generates an abnormal electric field

212 at ionospheric altitude. The distribution of ionospheric electric filed showed in Figure

213 8 were calculated by LAIC electric field penetration model proposed by *Zhou et al.*

214 (2017). Because of the existence of high conductivity of geomagnetic field, the

215 abnormal ionospheric electric filed could be mapped along geomagnetic field lines.

216 Geomagnetic conjugate ionospheric disturbances could be generated by abnormal

217 ionospheric electric filed through $E \times B$ drift. Our study provides observational

218 evidences of LAIC electric penetration rather than acoustic gravity wave mechanism.

219

220 Geomagnetic conjugate observations in ionosphere have been reported by a few

221 researchers. *Otsuka et al.* (2002; 2004) reported simultaneous observations of

222 equatorial airglow depletions and medium-scale TIDs at geomagnetic conjugate points

223 in both hemispheres by two all-sky imagers. Their results also suggested that

224 polarization electric field, which is important for airglow depletion and MSTIDs

225 generation, can be mapped along the field lines.

226

227 In our observations, we found that the ionospheric disturbances in both hemispheres

228 caused by the UNE-generated electric field penetration propagated radially at the

229   velocity of roughly 280 m/s in Figure 5 and Figure 7. LAIC electric field can be roughly

230   estimated to be 14.5 mV/m, which is consistent with the magnitude of the earthquake-

231   generated ionospheric electric field presented by *Zhang et al.* (2014). Figure 6 presents

232   the results of the ionospheric current disturbances detected by the satellite Swarm B

233   after the UNE. The reason may be that the ionospheric disturbances from the UNE

234   propagate here to generate the current disturbances by electrodynamic process.

235

236   Moreover, compared with the magnitude and time scale of ionospheric disturbances

237   caused by earthquakes, there are inconsistencies in our study. Based on IGS station

238   observations around Tibet and Nepal, *Kong et al.* (2018) reported that TEC disturbances

239   exceeded 0.3 TECU and lasted for 15-20 minutes during 2015 Nepal earthquake.

240   However, it was found that the UNE-generated ionospheric disturbances were relatively

241   smaller and lasted within 5 minutes in Figure 4. The reason for difference of TEC

242   disturbances may be that earthquake magnitude and background ionosphere are

243   different.

244

245   **5 Summary**

246   In this study, we have shown that the geomagnetic conjugate observations of GNSS

247   TEC and ionospheric current from Swarm considered as a response to North Korea

248   UNE on 3 September 2017. The LAIC electric penetration effects of UNE have been

249   discussed in details. The main results are summarized as follows:

250

12

1. The ionospheric TEC and current disturbances were observed in both hemispheres after the UNE. According to the spatial-temporal relation, UNE-generated ionospheric disturbances propagated radially from the explosion epicenter with the velocity of ~ 280 m/s.

2. The ionospheric disturbances may be caused by LAIC electric penetration rather than AGWs. LAIC electric field induced by UNE penetrates into the ionosphere and causes plasma density disturbances near the nuclear test cite and its conjugate points by electrodynamic process.

267 **References**

268 Che, I.-Y., Kim, T. S., Jeon, J.-S., and Lee, H.-I.: Infrasound observation of the apparent

269   North Korean nuclear test of 25 May 2009, Geophys. Res. Lett., 36, L22802, 2009.

270 Chum, J., Cabrera, M. A., Mošna, Z., Fagre, M., Baše, J., and Fišer, J.: Nonlinear

271   acoustic waves in the viscous thermosphere and ionosphere above earthquake, J.

272   Geophys. Res. Space Physics, 121, 2016.

273 Chum, J., Liu, J.-Y., Podolská, K., and Šindelářová, T.: Infrasound in the ionosphere

274   from earthquakes and typhoons, J. Atmos. Sol. Terr. Phys., 171, 72-82, 2018.

275 Garrison, J. L., Yang, Y.-M., and Lee, S.-C.: Observations of ionospheric disturbances

276   coincident with North Korean underground nuclear tests, Abstract SA43B-1754

277   presented at 2010 Fall Meeting, AGU, San Francisco, Calif., 13–17 Dec, 2010.

278 Gokhberg, M. B., Pilipenlco, V. A., Pokhotelov, O. A., and Partasaraty, S.: Acoustic

279   disturbance induced by underground nuclear explosion as source of electrostatic

280   turbulence in the magnetosphere, Doklady AN SSSR, 313(N3), P568-574, 1990.

281 Gousheva, M., Danov, D., Hristov, P., and Matova, M.: Quasi-static electric fields

282   phenomena in the ionosphere associated with pre- and post-earthquake effects, Nat.

283   Hazards Earth Syst. Sci., 8, 101-107, 2008.

284 Gousheva, M., Danov, D., Hristov, P., and Matova, M.: Ionospheric quasi-static electric

285   field anomalies during seismic activity in August–September 1981, Nat. Hazards

286   Earth Syst. Sci., 9, 3-15, 2009.

287 Huang, Q.: Retrospective investigation of geophysical data possibly associated with the

288   Ms8.0 Wenchuan earthquake in Sichuan, China, J. Asian Earth Sci., 41(4-5): 421-

289   427, 2011.

290   Jonah, O. F., Kherani, E. A., and De Paula, E. R.: Investigations of conjugate MSTIDS

291   over the Brazilian sector during daytime, J. Geophys. Res. Space Physics, 122.

292   9576-9587, 2017.

293   Klimenko, M. V., Klimenko, V. V., Karpov, I. V., and Zakharenkova, I. E.: Simulation

294   of Seismo-Ionospheric Effects Initiated by Internal Gravity Waves, Russ. J. Phys.

295   Chem. B, 5(3), 393-401, 2011.

296   Kong, J., Yao, Y., Zhou, C., Liu, Y., Zhai, C., Wang, Z., and Liu, L.: Tridimensional

297   reconstruction of the Co-Seismic Ionospheric Disturbance around the time of 2015

298   Nepal earthquake, J. Geodesy, 3, 1-12, 2018.

299   Li, M., and Parrot, M.: Statistical analysis of the ionospheric ion density recorded by

300   DEMETER in the epicenter areas of earthquakes as well as in their magnetically

301   conjugate point area, Adv. Space Res., 61(3), 974-984, 2017.

302   Liu, J. Y., Le, H., Chen, Y. I., Chen, C. H., Liu, L., Wan, W., Su, Y. Z., Sun, Y. Y., Lin,

303   C. H., and Chen, M. Q.: Observations and simulations of seismo-ionospheric GPS

304   total electron content anomalies before the 12 January 2010 M7 Haiti earthquake,

305   J. Geophys. Res., 116, A04302, 2011.

306   Liu, J. Y., Chen, C. H., Sun, Y. Y., Chen, C. H., Tsai, H. F., Yen, H. Y., Chum, J.,

307   Lastovicka, J., Yang, Q. S., Chen, W. S., and Wen, S.: The vertical propagation of

308   disturbances triggered by seismic waves of the 11 March 2011 M9.0 Tohoku

309   earthquake over Taiwan, Geophys. Res. Lett., 43(4), 1759-1765, 2016.

310   Maruyama, T., Yusupov, K., and Akchurin, A.: Ionosonde tracking of infrasound

311   wavefronts in the thermosphere launched by seismic waves after the 2010 M8.8

312   Chile earthquake, J. Geophys. Res. Space Physics., 121, 2683-2692, 2016.

313 Mikhailov, Y. M., Mikhailova, G. A., and Kapustina, O. V.: VLF effects in the outer

314   ionosphere from the underground nuclear explosion on Novaya Zemlya island on

315   24 October, 1990 (INTERCOSMOS 24 satellite data), Phys. Chem. Earth Part C,

316   25(1–2), 93–96, 2000.

317 Otsuka, Y., Shiokawa, K., Ogawa, T., and Wilkinson, P.: Geomagnetic conjugate

318   observations of equatorial airglow depletions, Geophys. Res. Lett., *29*, 1753, 2002.

319 Otsuka, Y., Shiokawa, K., Ogawa, T., and Wilkinson, P.: Geomagnetic conjugate

320   observations of medium-scale traveling ionospheric disturbances at midlatitude

321   using all-sky airglow imagers, Geophys. Res. Lett., 31, L15803, 2004.

322 Park, J., Frese, R. R. B. von, Grejner-Brzezinska, D. A., Morton, Y., and Gaya-Pique,

323   L. R.: Ionospheric detection of the 25 May 2009 North Korean underground

324   nuclear test, Geophys. Res. Lett., 38, L22802, 2011.

325 Park, J., Helmboldt, J., Grejner-Brzezinska, D. A., Frese, R. R. B. von, and Wilson, T.

326   L.: Ionospheric observations of underground nuclear explosions (UNE) using GPS

327   and the Very Large Array, Radio Sci., 48, 463–469, 2013.

328 Pokhotelov, O. A., Pilipenko, V. A., Fedorov, E. N., Stenflo, L., and Shukla, P. K.:

329   Induced electromagnetic turbulence in the ionosphere and the magnetosphere,

330   Physica Scripta, 50, 600-605, 1994.

331 Pokhotelov, O. A., Parrot, M., Pilipenko, V. A., Fedorov, E. N., Surkov V. V., and

332   Gladyshev V. A.: Response of the ionosphere to natural and man-made acoustic

333   sources, Ann. Geophys., 13, N11, 1197- 1210, 1995.

334 Pokhotelov, O. A., Pilipenko, V. A., and Parrot, M.: Strong atmospheric disturbances

335   as a possible origin of inner zone particle diffusion, Ann. Geophys., 17, 526-532,

336   1999.

337 Pulinets, S. A., Boyarchuk, K. A., Hegai, V. V., Kim, V. P., and Lomonosov, A. M.:

338   Quasi-electrostatic model of atmosphere-thermosphere-ionosphere coupling, Adv.

339   Space Res., 26(8), 1209-1218, 2000.

340 Ritter, P., Lühr, H., and Rauberg, J.: Determining field-aligned currents with the Swarm

341   constellation mission, Earth Planets Space, 65, 1285-1294, 2013.

342 Ruzhin, Y. Y., Larkina, V. I., and Depueva, A. K.: Earthquake precursors in

343   magnetically conjugated ionosphere regions, Adv. Space Res., 21(3), 525-528,

344   1998.

345 Sorokin, V. M., Chmyrev, V. M., and Yaschenko, A. K.: Electrodynamic model of the

346   lower atmosphere and the ionosphere coupling, J. Atmos. Sol. Terr. Phys., 63(16),

347   1681-1691, 2001.

348 Xu, T., Hu, Y., Wu, J., Wu, Z., Li, C., Xu, Z., and Suo, Y.: Anomalous enhancement of

349   electric field derived from ionosonde data before the great Wenchuan earthquake,

350   Adv. Space Res., 47(6), 1001-1005, 2011.

351 Yang, Y.-M., Garrison, J. L., and Lee, S. C.: Ionospheric disturbances observed

352   coincident with the 2006 and 2009 North Korean underground nuclear tests,

353   Geophys. Res. Lett., 39, L02103, 2012.

354 Zhao, B., and Hao, Y.: Ionospheric and geomagnetic disturbances caused by the 2008

355   Wenchuan earthquake: A revisit, J. Geophys. Res. Space Phys., 120, 5758–5777,

356   2015.

357 Zhang, X., Shen, X., Liu, J., Ouyang, X., Qian, J., and Zhao, S.: Analysis of ionospheric

358   plasma perturbations before Wenchuan earthquake, Nat. Hazards Earth Syst. Sci.,

359   9, 1259-1266, 2009.

360 Zhang, X., Shen, X., Zhao, S., Yao, L., Ouyang, X., and Qian, J.: The characteristics of

361   quasistatic electric field perturbations observed by DEMETER satellite before

362   large earthquakes, J. Asian Earth Sci., 79(2), 42-52, 2014.

363 Zhou, C., Liu, Y., Zhao, S., Liu, J., Zhang, X., Huang, J., Shen, X., Ni, B., and Zhao,

364   Z.: An electric field penetration model for seismo-ionospheric research, Adv.

365   Space Res., 60(10), 2217-2232, 2017.

366

367

368

369

Figure Captions

Figure 1. The positions of UNE and IGS stations. The position of 3 September 2017

North Korea UNE is represented by black hollow start mark. The locations of IGS

stations in both hemispheres are represented by red and blue squares, respectively.

Lines of constant geomagnetic latitude are represented by black dashed lines.

Figure 2. An example of time series of relative STEC obtained by SUWN using

satellite PRN 28 between 03:00-05:00 UT on 3 September 2017. The explosive time is

represented by the red line.

Figure 3. The time sequences of derivatives of relative STEC obtained by SUWN

station using satellite PRN 28 between 03:00-05:00 UT on 3 September 2017. (a) first-

order derivatives, (2) second-order derivatives, (c) third-order derivatives, and (d)

wavelet de-noised third-order derivatives. The explosive time is represented by the red

line.

Figure 4. The time sequences of 3-order derivatives of carrier phase derived relative

STEC by GNSS observations from different IGS stations in East Asia (left and middle

column) and Australia (right column) on 3 September 2017. The blue lines indicate the

wavelet de-noised 3-order derivative of relative STEC. The black lines indicate the GPS

signal's elevation between the GNSS satellite and IGS stations. The explosive time is

represented by the red line.

Figure 5. The IPPs tracks of relative STEC derivatives. The red lines indicate the IPPs

tracks obtained by IGS stations in the northern hemisphere. The blue lines indicate the

magnetic conjugate positions of the IPPs tracks obtained by IGS stations in the southern

hemisphere. The positions of the maximum amplitudes of relative STEC derivatives in

the northern hemisphere are represented by red triangles. The geomagnetic conjugate

positions of the maximum amplitudes of relative STEC derivatives in the southern

hemisphere are represented by blue triangles.

Figure 6. Results of Swarm B ionospheric current data analysis for the 2017 UNE: (a),

(c), and (e) are the FAC, (b), (d), (f) are the IRC. From top to bottom, they indicate

observations of Swarm B on 19 August 2017 (quiet time), 3 September 2017 (UNE

399   time), and 18 September 2017 (quiet time), respectively. The ionospheric current

400   disturbances in response to UNE are represented by the red rectangles.
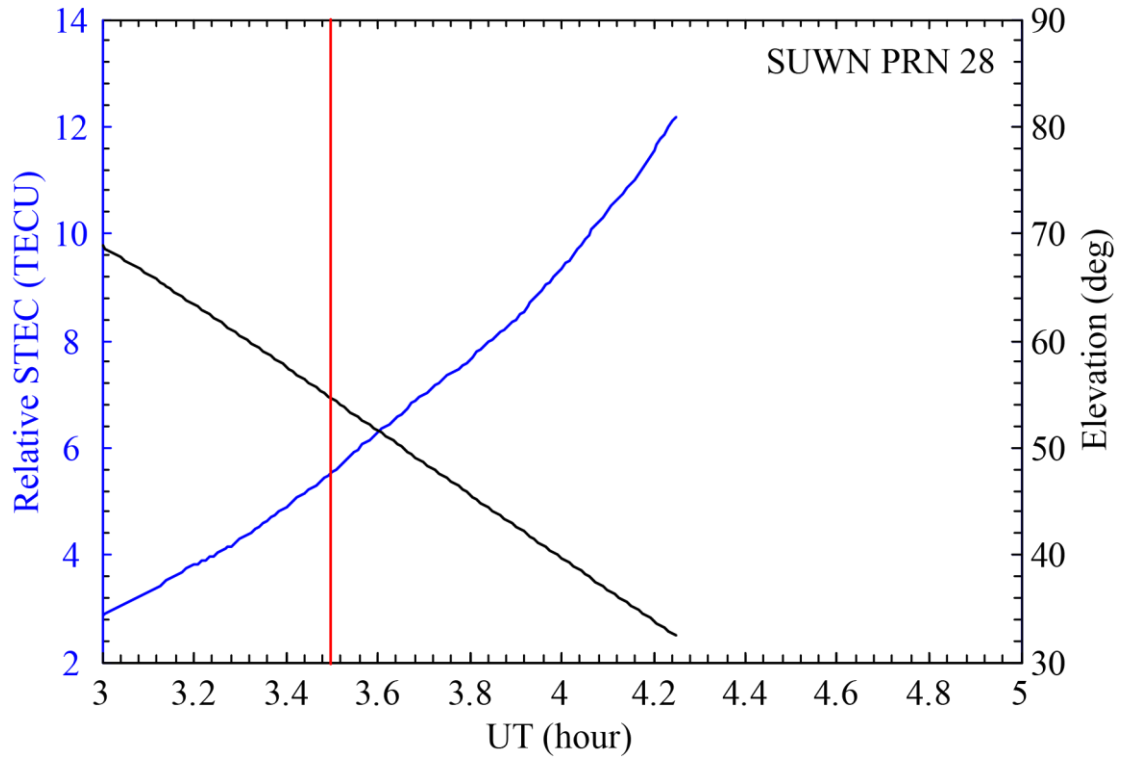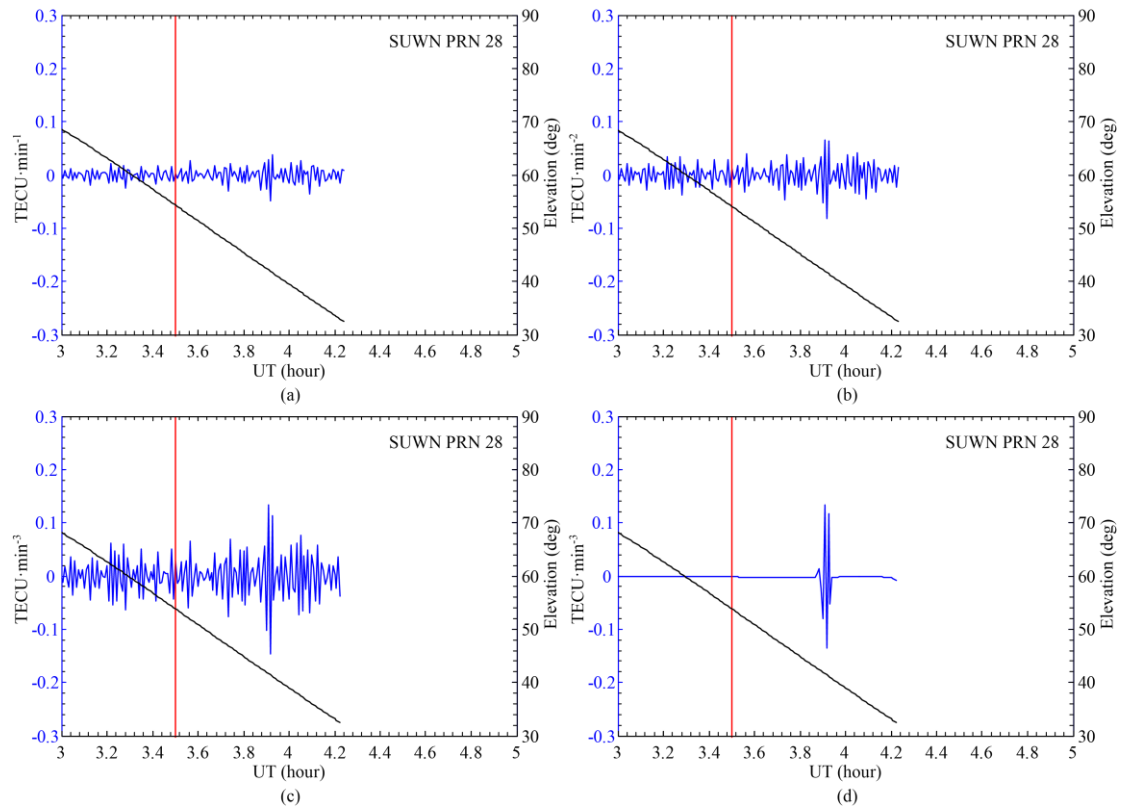
401   **Figure 7.** Horizontal distance-time data for the UNE-generated ionospheric

402   disturbances. The black line indicates the fitting curve obtained by the least square

403   method. The gray lines represent the boundaries of 95% confidence intervals. The red

404   and blue triangles indicate same meanings as in Figure 5. The black triangle represents

405   the position of ionospheric current disturbances in the northern hemisphere. The green

406   triangle represents the geomagnetic conjugate position of ionospheric current

407   disturbances in the southern hemisphere.

408   **Figure 8.** A sketch of geomagnetic conjugate effect related to UNE in the region of the

409   nuclear test site nearby and the corresponding geomagnetic conjugate region.
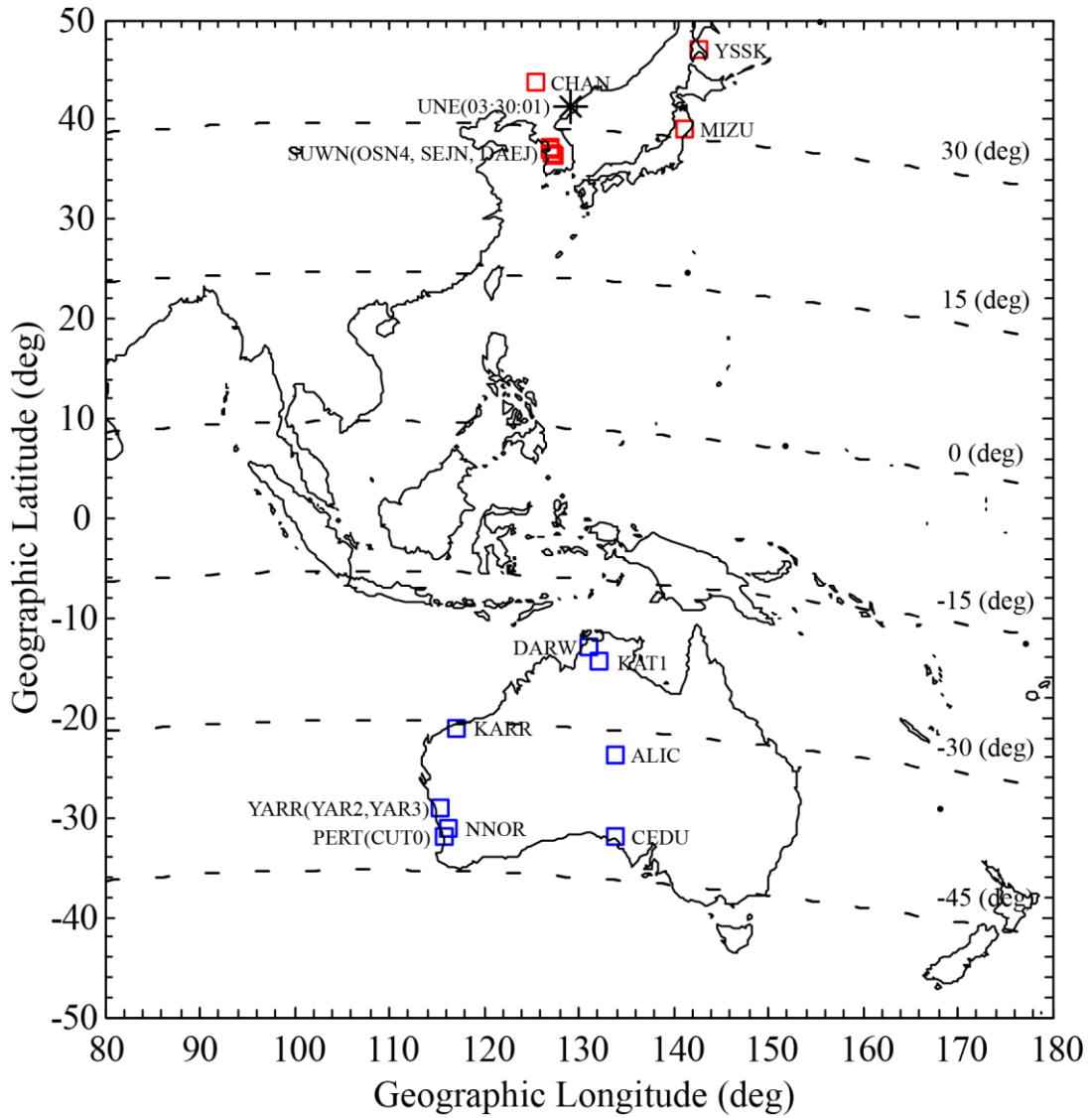
Figure 1. The positions of UNE and IGS stations. The position of 3 September 2017 North Korea UNE is represented by black hollow start mark. The locations of IGS stations in both hemisphere are represented by red and blue squares, respectively. Lines of constant geomagnetic latitude are represented by black dashed lines.
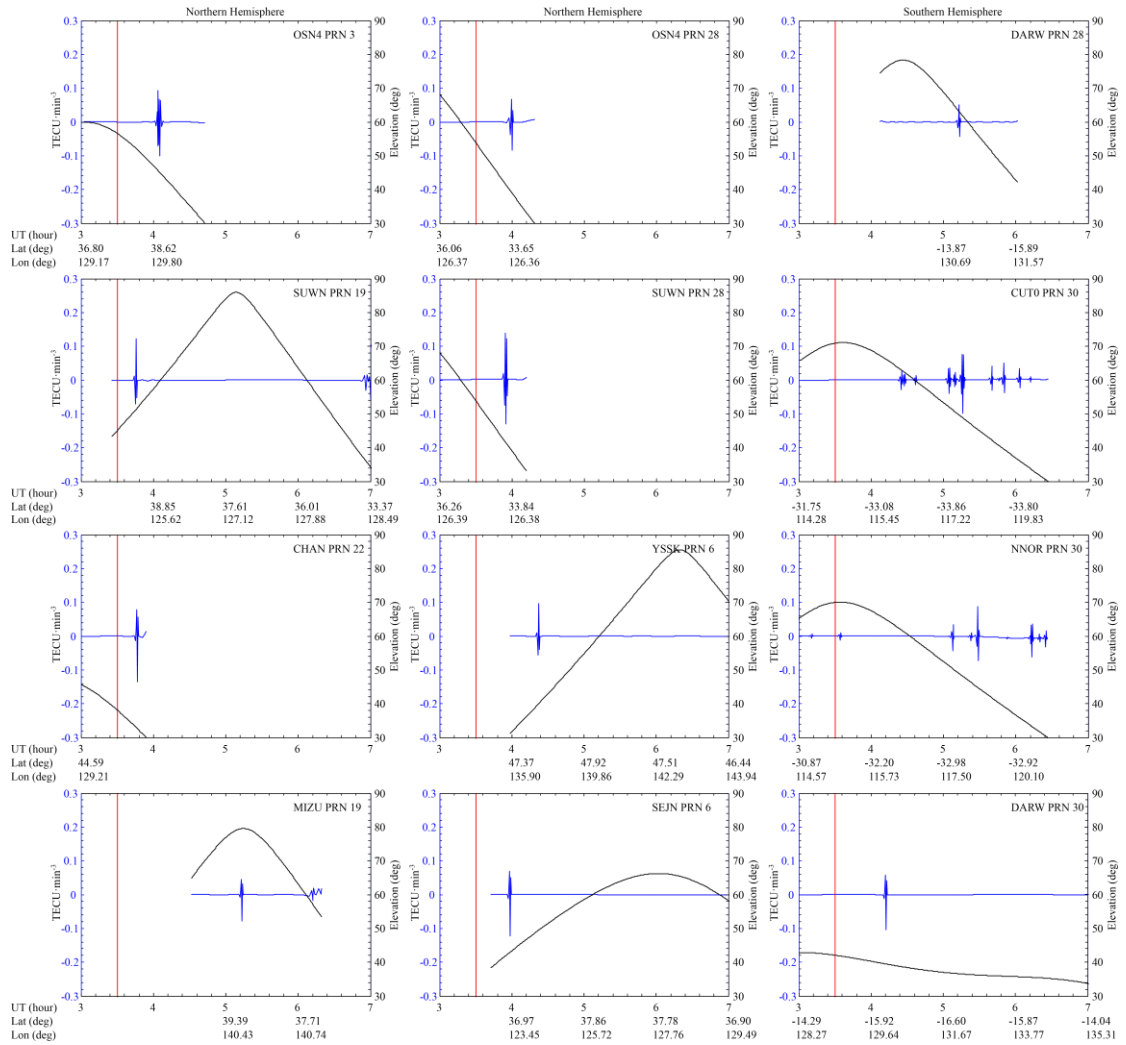
418

Figure 2. An example of time series of relative STEC obtained by SUWN using

satellite PRN 28 between 03:00-05:00 UT on 3 September 2017. The explosive time

is represented by the red line.

Figure 3. The time sequences of derivatives of relative STEC obtained by SUWN station using satellite PRN 28 between 03:00-05:00 UT on 3 September 2017. (a) first-order derivatives, (2) second-order derivatives, (c) third-order derivatives, and (d) wavelet de-noised third-order derivatives. The explosive time is represented by the red line.

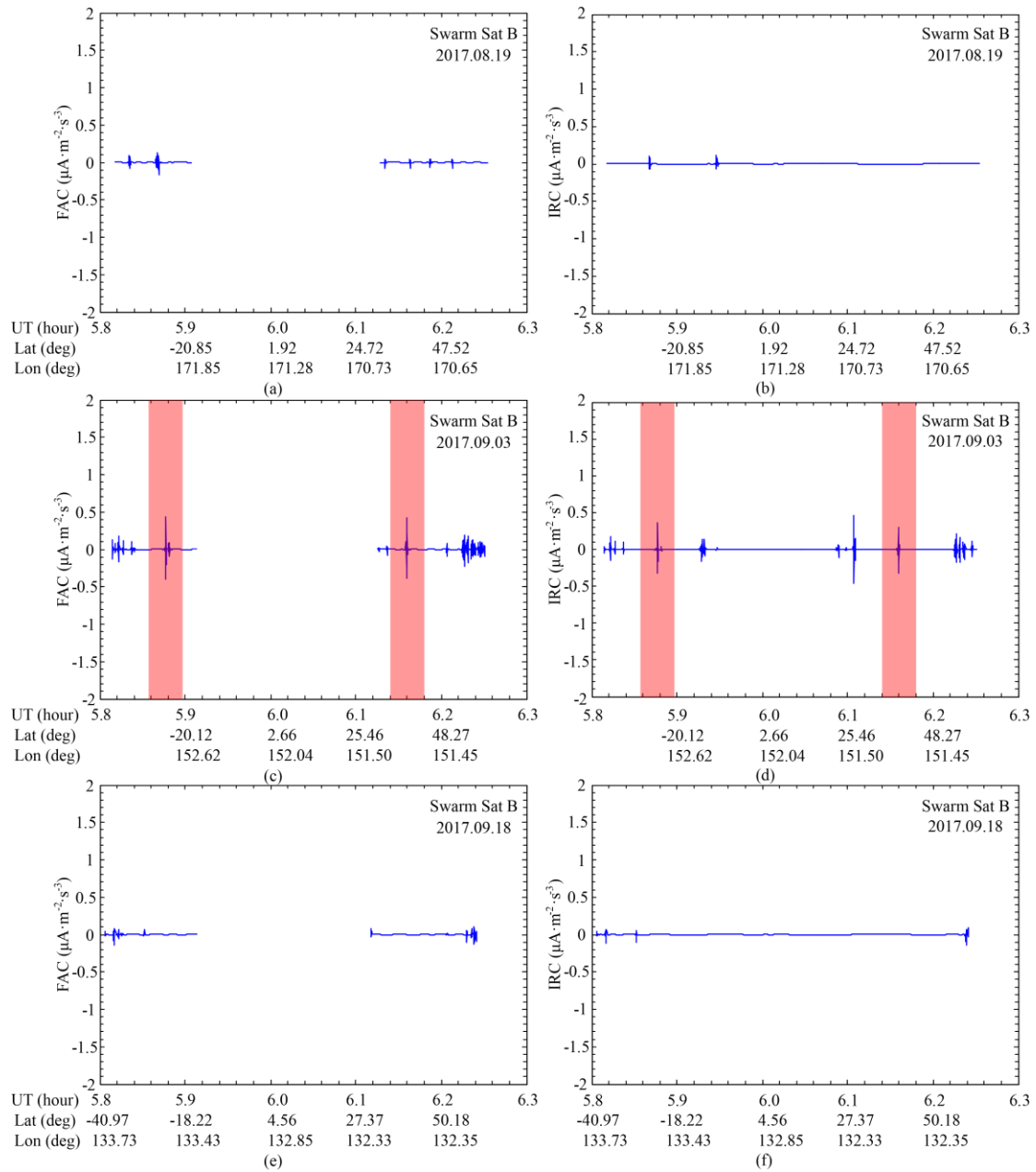**Figure 4.** The time sequences of 3-order derivatives of carrier phase derived relative STEC by GNSS observations from different IGS stations in East Asia (left and middle column) and Australia (right column) on 3 September 2017. The blue lines indicate the wavelet de-noised 3-order derivative of relative STEC. The black lines indicate the GPS signal's elevation angle between the GNSS satellite and IGS stations. The explosive time is represented by the red line.

Figure 5. The IPPs tracks of relative STEC derivatives. The red lines indicate the IPPs tracks obtained by IGS stations in the northern hemisphere. The blue lines indicate the magnetic conjugate positions of the IPPs tracks obtained by IGS stations in the southern hemisphere. The positions of the maximum amplitudes of relative STEC derivatives in the northern hemisphere are represented by red triangles. The geomagnetic conjugate positions of the maximum amplitudes of relative STEC derivatives in the southern hemisphere are represented by blue triangles.
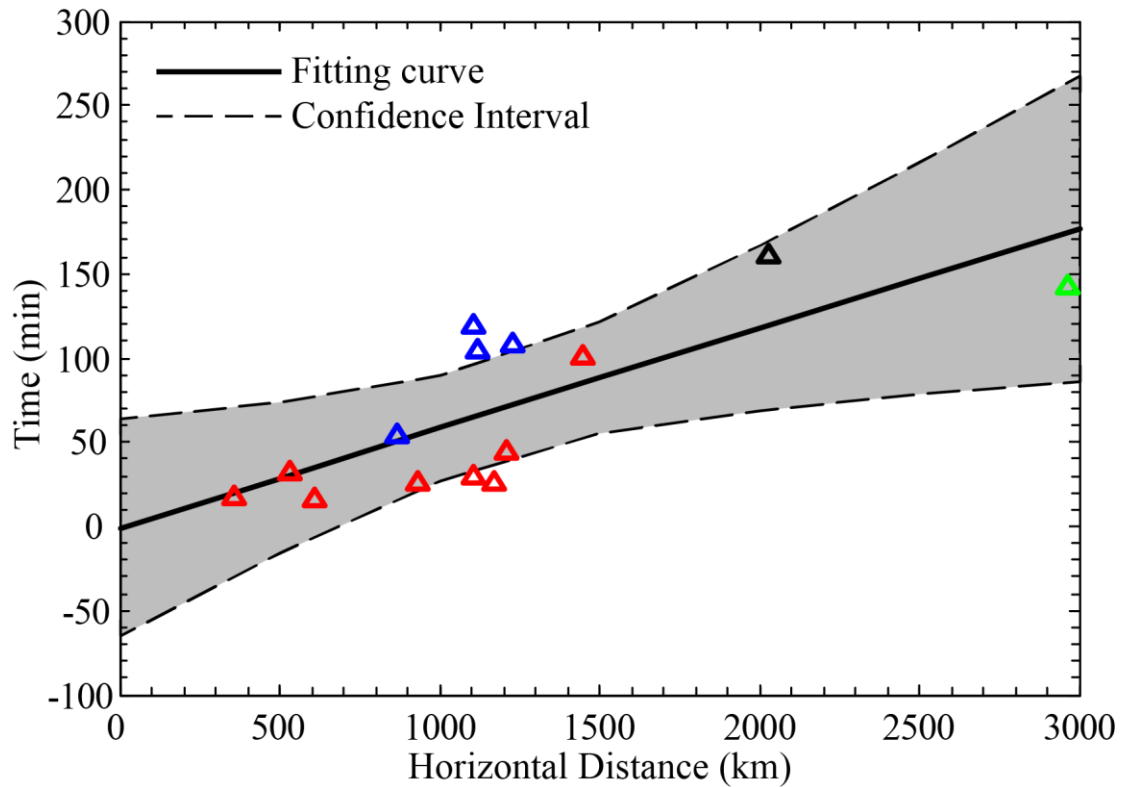
Figure 6. Results of Swarm B ionospheric current data analysis for the 2017 UNE: (a), (c), and (e) are the FAC, (b), (d), (f) are the IRC. From top to bottom, they indicate observations of Swarm B on 19 August 2017 (quiet time), 3 September 2017 (UNE time), and 18 September 2017 (quiet time), respectively. The ionospheric current disturbances in response to UNE are represented by the red rectangles.

Figure 7. Horizontal distance-time data for the UNE-generated ionospheric disturbances. The black line indicates the fitting curve obtained by the least square method. The gray lines represent the boundaries of 95% confidence intervals. The red and blue triangles indicate same meanings as in Figure 5. The black triangle represents the position of io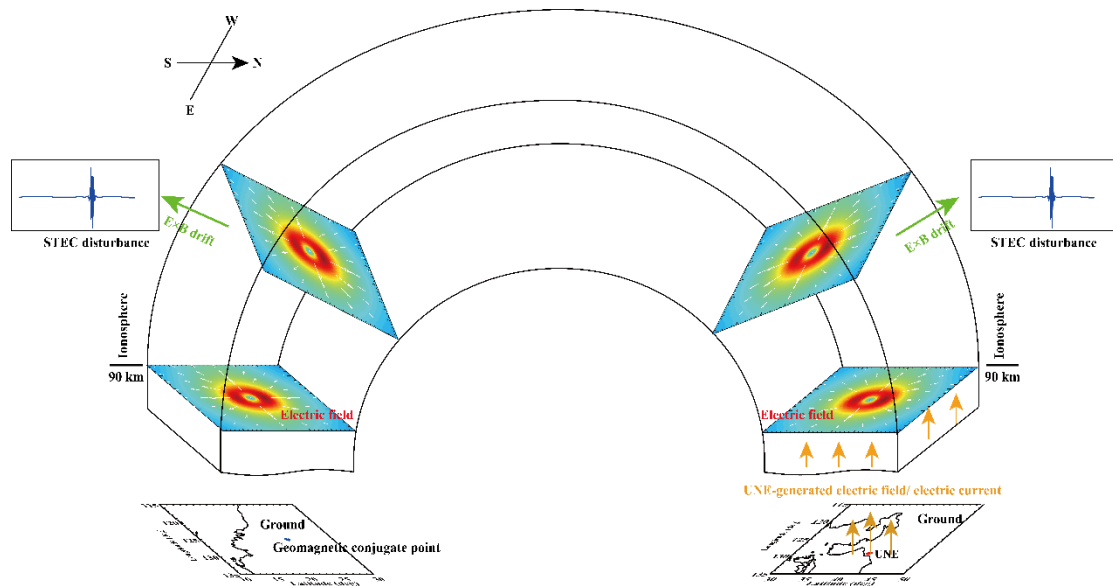nospheric current disturbances in the northern hemisphere. The green triangle represents the geomagnetic conjugate position of ionospheric current disturbances in the southern hemisphere.

459

460 **Figure 8.** A sketch of geomagnetic conjugate effect related to UNE in the region of

461 the nuclear test site nearby and the corresponding geomagnetic conjugate region.